Winding-Number Measurements in a Noisy Quantum Simulation

Keyan Liu(刘可岩) and Wen-Long You(尤文龙)*

Center for the Cross-disciplinary Research of Space Science and Quantum-technologies, College of Physics, Nanjing University of Aeronautics and Astronautics, Nanjing 211106, China

Abstract

We demonstrate a shallow-circuit approach to topological measurements in an extended transverse-field Ising chain by measuring the transverse magnetization and finite-grid winding number with 16 and 32 qubits on the Tianyan-176 superconducting processor. Independent momentum pairs are prepared in parallel, and single-qubit Z components and two-qubit XX correlations give both observables without an inverse fermionic Fourier transformation. Although the measured magnetization deviates from the ideal result, 99.1% of the individual winding-number measurements reproduce the ideal finite-grid value. The few incorrect results occur near phase transitions, where pseudospins at neighboring points of the finite momentum grid become nearly antiparallel and small errors can change the winding number by one. Noise simulations show that increasing the number of shots reduces finite-shot errors but does not correct noise-induced changes in the mean pseudospin directions.

Keywords: quantum simulation, transverse-field Ising chain, winding number, shallow quantum circuits
PACS: 03.67.Lx, 75.10.Pq, 03.65.Vf

1. Introduction

The transverse-field Ising chain (TFIC) provides an exactly solvable model of a quantum phase transition [1,2]. Its quadratic fermion representation permits quantum-circuit implementations with analytically known eigenstates and observable expectation values [3,4]. Gate errors and decoherence limit the circuit depth accessible on noisy intermediate-scale quantum devices [5,6], motivating schemes that prepare only the correlations required for the observables of interest.

Exact circuits for Ising and XY chains prepare real-space eigenstates by reversing the Jordan–Wigner, fermionic Fourier, and Bogoliubov transformations [3,4,7]. Compressed encodings [8,9] and algebraic compression of free-fermion evolution circuits [10] reduce their resource requirements. Alternatively, independent momentum sectors can be simulated directly, as demonstrated for dynamical phase transitions on a superconducting qubit [11]. Constant-depth circuits have also been used to study magnetization dynamics and Majorana modes in the transverse-field Ising chain on a superconducting quantum processor [12]. Momentum-state lattices in ultracold atoms provide an alternative platform for studying topology, localization, and chiral dynamics [13–15].

Adding a three-spin cluster interaction preserves the quadratic structure of the TFIC and produces phases with winding numbers zero, one, and two [16]. These phases can be characterized by pseudospin winding and Majorana edge modes [17,18]. Related cluster–Ising models also exhibit geometric-phase scaling and multicritical behavior [19,20]. Translation invariance separates the model into independent pairs of opposite momenta [21]. The transverse magnetization follows from the momentum occupations, whereas the winding number is determined by the momentum-resolved pseudospin directions. Encoding each $(k, -k)$ pair in two qubits therefore gives direct access to both observables without implementing an inverse fermionic Fourier transformation. Experiments have measured topological properties of cluster–Ising chains [22] and accessed topological invariants through quantum-geometric measurements and quantum walks [23,24]. Momentum-selective tomography has also been used to measure winding numbers of an extended SSH model on a superconducting processor [25].

Previous hardware studies extracted topological phase boundaries from entanglement observables using symmetry-preserving momentum sampling [26] and measured wave-function topology from overlaps between neighboring parameter points, including analyses of gate noise and finite-shot fluctuations [27]. For direct pseudospin measurements, an integer result does not by itself establish agreement with the ideal winding number. Magnetization depends on pseudospin components, whereas a finite-grid winding number depends on the angles between neighboring pseudospins on the finite momentum grid. When these directions are nearly opposite, a small measurement error can carry the phase difference through $+\pi$ or $-\pi$ and change the finite-grid winding number by one, even though every pseudospin remains nonzero. We examine when such directional errors leave

*Corresponding author. E-mail: wlyou@nuaa.edu.cn

the finite-grid winding number unchanged and whether increasing the number of measurements can reduce the resulting errors. This requires distinguishing fluctuations due to a finite number of measurements from noise-induced changes in the mean pseudospin directions.

Here we measure magnetization and winding numbers in an extended TFIC using momentum-pair circuits on Tianyan-176 with 16 and 32 qubits [28,29]. The approach combines parallel preparation of independent momentum pairs with an angular stability criterion on the finite momentum grid and a comparison of finite-shot reconstructions with the winding of the mean noisy pseudospins. Of 340 individual runs, 337 yield the ideal finite-grid winding number despite deviations in the measured magnetization. The three incorrect values arise when phase differences between neighboring sampled momenta cross π as the corresponding pseudospins become antiparallel. Noise simulations separate finite-shot fluctuations from noise-induced changes in the mean pseudospin directions. Once noise changes the winding number of the mean pseudospins, increasing the shot count concentrates the results around an incorrect winding number.

2. Model and quantum circuits

We consider an extended TFIC with an even number N of spins and periodic boundary conditions [16,17],

$$H = -\sum_{j=1}^{N} \left(g\sigma_j^x + \lambda_1 \sigma_j^z \sigma_{j+1}^z + \lambda_2 \sigma_j^x \sigma_{j-1}^z \sigma_{j+1}^z \right). \tag{1}$$

Here g is the transverse field, λ_1 and λ_2 are the Ising and three-spin couplings, and $\sigma_{j+N}^{\alpha} = \sigma_j^{\alpha}$. The standard TFIC is recovered at $\lambda_2 = 0$. In the experimental and numerical results below, we take the transverse field g as the energy unit and set $g = 1$. Accordingly, λ_1 and λ_2 are given in units of g. The Jordan–Wigner transformation

$$c_j = \left(\prod_{l<j} \sigma_l^x \right) \frac{\sigma_j^z - \mathrm{i}\sigma_j^y}{2}, \qquad \sigma_j^x = 1 - 2c_j^\dagger c_j \tag{2}$$

maps the interactions to nearest- and next-nearest-neighbor fermionic hopping and pairing. We work in the even fermion-parity sector, where periodic spins give antiperiodic fermionic boundary conditions (APBC), $c_{j+N} = -c_j$ [1,30]. We use the Fourier transformation

$$c_j = \frac{e^{\mathrm{i}\pi/4}}{\sqrt{N}} \sum_k e^{-\mathrm{i}kj} c_k, \tag{3}$$

where k runs over the APBC momenta $k_m = -\pi + 2\pi(m + 1/2)/N$, with $m = 0, \ldots, N-1$, for unit lattice spacing. The momenta occur in opposite pairs $(k, -k)$. We use k as the momentum variable below and reserve k_m for the ordered finite-size momentum grid. The fixed phase $e^{\mathrm{i}\pi/4}$ is a fermionic gauge choice that allows the pair ground state to be written with real coefficients.

In the Nambu basis $\Psi_k = (c_k, c_{-k}^\dagger)^T$, the Hamiltonian separates into $N/2$ independent $(k, -k)$ sectors with $0 < k < \pi$,

$$H = 2 \sum_{0<k<\pi} \Psi_k^\dagger h(k) \Psi_k. \tag{4}$$

The Bogoliubov–de Gennes (BdG) matrix is $h(k) = d_z(k)\tau_z + d_x(k)\tau_x$, where τ_α act in particle–hole space, $d_z(k) = g - \lambda_1 \cos k - \lambda_2 \cos(2k)$, and $d_x(k) = \lambda_1 \sin k + \lambda_2 \sin(2k)$. Its eigenvalues are $\pm E(k)$, with $E(k) = \sqrt{d_z(k)^2 + d_x(k)^2}$, so that the quasiparticle excitation energy is $2E(k)$.

The momentum dependence of $d_x(k)$ and $d_z(k)$ defines the pseudospin angle $\theta_k = \arg[d_z(k) - \mathrm{i}d_x(k)]$, where the phase is continuously unwrapped along the Brillouin zone. For a gapped system, the winding number is

$$\nu = \frac{1}{2\pi} \int_0^{2\pi} \partial_k \theta_k \, \mathrm{d}k. \tag{5}$$

The $\cos(2k)$ and $\sin(2k)$ terms generated by λ_2 allow the pseudospin trajectory to wind twice around the origin, giving $\nu = 0, 1, 2$ [16,17]. Changing ν requires a gap closing, $d_z = d_x = 0$.

Figure 1 shows the phase diagram of the extended TFIC in the thermodynamic limit. For $0 \le \lambda_1 \le 2$, the gap closes along $\lambda_2 = 1 - \lambda_1$, $\lambda_2 = 1 + \lambda_1$, and $\lambda_2 = -1$, separating regions with winding numbers $\nu = 0, 1$, and 2. The measurements below follow two one-dimensional cuts, $\lambda_2 = 0$ and $\lambda_1 = 0.5$. The former crosses the boundary between $\nu = 0$ and 1, whereas the latter gives the sequence $\nu = 2 \to 0 \to 1 \to 2$. These thermodynamic-limit boundaries serve as references for the measurements. Owing to finite momentum sampling, the finite-grid winding number ν_N can change at parameter values that differ from these boundaries.

For each $(k, -k)$ sector, the many-body ground state lies in the even-parity subspace spanned by $|00\rangle$ and $|11\rangle = c_k^\dagger c_{-k}^\dagger |00\rangle$. For $E(k) > 0$, the pair ground state is

$$|g_k\rangle = \cos\frac{\theta_k}{2}|00\rangle + \sin\frac{\theta_k}{2}|11\rangle. \tag{6}$$

Although this ideal state can be represented by one logical qubit, we use two physical qubits to retain a separate occupation for each momentum mode. The mode occupations and pairing correlation are then directly accessible through Z_1,

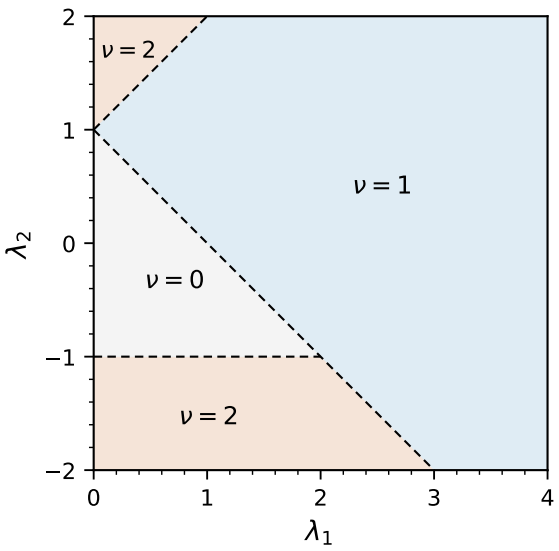


Fig. 1. Phase diagram of the extended transverse-field Ising chain in the thermodynamic limit. The regions are labeled by the winding number $\nu = 0, 1$, and 2, and the black dashed lines mark the gap-closing boundaries.

Z_2, and X_1X_2, respectively, and joint measurement counts retain the correlations between the occupation estimates under noise.

The pair ground state in Eq. (6) can be prepared directly from $|00\rangle$. A rotation $R_y(\theta_k)$ on the first qubit sets the two amplitudes. A subsequent controlled-NOT gate, with the first qubit as the control, prepares $|g_k\rangle$ [3,4,7,31]. Since the $(k, -k)$ sectors are independent, all momentum pairs can be assigned to disjoint qubit pairs and prepared in parallel, as shown in Fig. 2(a,b). The $N = 16$ and $N = 32$ implementations therefore require 8 and 16 two-qubit gates, respectively, arranged in a single entangling layer. The selected qubits and couplings for $N = 16$ are shown in Fig. 2(c). The circuit structure remains unchanged throughout the parameter scans, and the model parameters enter only through the rotation angles θ_k.

If the momentum pairs occupy disjoint physical couplings that support simultaneous gates, preparing $N/2$ pairs requires $N/2$ entangling gates in a single layer. On Tianyan-176, each CNOT gate is implemented using one native CZ gate together with single-qubit gates. Increasing the momentum resolution therefore requires more parallel qubit pairs, but no additional entangling layers. The available disjoint couplings and native CZ gates on Tianyan-176 therefore match the pairwise circuit structure: each pair uses one native entangling gate, and no routing between different pairs is required.

For each momentum pair, qubits 1 and 2 represent the occupations of the k and $-k$ modes, respectively, and X_a and Z_a denote the Pauli

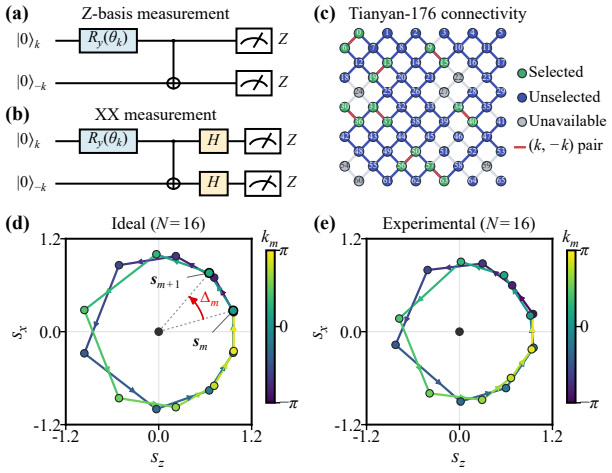


Fig. 2. Momentum-pair circuits and winding-number measurement. **(a,b)** Preparation of the $(k, -k)$ pair ground state and measurement of the longitudinal components in the computational basis (a) and the XX correlation (b). The first and second qubits represent the k and $-k$ modes, respectively. **(c)** Tianyan-176 connectivity. The 16 selected qubits are shown in green, with the eight couplings used for parallel pair preparation shown in red. **(d,e)** Ideal (d) and experimental (e) pseudospin textures for $N = 16$, $\lambda_1 = 0.5$, and $\lambda_2 = -2$. Each point denotes $s_m = s_z(k_m) + \mathrm{i}s_x(k_m)$ at an APBC momentum k_m, with neighboring momenta connected in increasing-k order. The color scale denotes k_m, and the arrows indicate increasing momentum. The red dashed arc in (d) denotes the signed angular increment Δ_m between neighboring pseudospins. The experimental data use 1,000 shots in each measurement basis. The winding numbers are $\nu_N = 2$ and $\nu_N^{\mathrm{exp}} = 2$, respectively.

operators acting on qubit $a = 1, 2$. For the ground state in Eq. (6), the pseudospin components are $s_z(k) = \langle g_k|Z_1|g_k\rangle = d_z(k)/E(k)$ and $s_x(k) = \langle g_k|X_1X_2|g_k\rangle = -d_x(k)/E(k)$. The longitudinal components are obtained by measuring the two qubits in the computational basis, while the transverse component is obtained from the correlation $\langle X_1X_2\rangle$ after applying a Hadamard gate to each qubit.

To calculate the winding number, we represent the planar pseudospin by $s(k) = s_z(k) + \mathrm{i}s_x(k) = [d_z(k) - \mathrm{i}d_x(k)]/E(k)$. For the ideal ground state, $s(k) = e^{\mathrm{i}\theta_k}$. Since $d_z(k)$ is even and $d_x(k)$ is odd under $k \to -k$, the ideal pseudospin texture has momentum-inversion symmetry, $s_z(-k) = s_z(k)$ and $s_x(-k) = -s_x(k)$, or equivalently $s(-k) = s(k)^*$. For each $(k, -k)$ pair, the transverse components are obtained from the same measured XX correlation with opposite signs, while $s_z(k)$ and $s_z(-k)$ are extracted from the same two-qubit Z-basis counts. The transverse magnetization is defined as $M_x = N^{-1}\sum_j\langle\sigma_j^x\rangle$. It is also determined by the longitudinal pseudospin component. Using the Jordan–Wigner relation $\sigma_j^x = 1 - 2c_j^\dagger c_j$ and the invariance of the total fermion occupation under the Fourier transformation gives $M_x = 1 - \frac{2}{N}\sum_k\langle c_k^\dagger c_k\rangle$. For the

pair ground state, $1 - 2\langle c_k^\dagger c_k\rangle = s_z(k)$, and hence $M_x = \frac{1}{N}\sum_{0<k<\pi}[s_z(k) + s_z(-k)]$.

For the finite chain, only the discrete APBC momenta k_m are available, and we write $s_m = s(k_m)$. The signed angular increment between neighboring pseudospins on the finite momentum grid is $\Delta_m = \mathrm{Arg}(s_{m+1}s_m^*)$, with $\mathrm{Arg} \in (-\pi, \pi]$. The phase difference between k_m and k_{m+1} is therefore reduced modulo 2π to this fixed interval, which defines its principal value. With cyclic indexing $s_N = s_0$, summing the increments around the Brillouin zone gives the finite-grid winding number

$$\nu_N = \frac{1}{2\pi}\sum_{m=0}^{N-1}\Delta_m. \tag{7}$$

Figure 2(d,e) shows the ideal and measured pseudospin textures for $N = 16$, $\lambda_1 = 0.5$, and $\lambda_2 = -2$. Both wind twice around the origin, corresponding to a total phase change of 4π.

For nonzero pseudospins whose directions at neighboring momenta are not antiparallel, this cyclic sum is integer-valued. It equals the bulk winding number ν if the continuously unwrapped phase changes by less than π in magnitude between every pair of adjacent sampled momenta. Near a gap closing, the direction can vary rapidly within a momentum interval that the grid does not resolve, giving $\nu_N \neq \nu$ even without measurement errors. Measurement noise can also drive a phase difference near either endpoint of $(-\pi, \pi]$ across that endpoint. Its principal value then jumps by 2π in magnitude, as discussed below.

Thus, the magnetization and winding number can both be obtained from the same momentum-pair states using the Z- and X-basis measurements described above, without implementing an inverse fermionic Fourier transformation.

3. Experimental measurements and winding-number errors

We implement the measurement scheme described above on Tianyan-176 [28,29] for $N = 16$ and $N = 32$. For each system size, 34 parameter points are sampled along two one-dimensional cuts in parameter space: varying λ_1 at $\lambda_2 = 0$ and varying λ_2 at $\lambda_1 = 0.5$. At each parameter point, we perform five independent runs. In each run, we use 1,000 shots in the Z basis and 1,000 shots in the X basis to measure the longitudinal components and the XX correlation, respectively. Every shot consists of state preparation followed by measurement in the chosen basis. For M_x^{exp}, the measured longitudinal components at k and $-k$ are used separately in the average over all N momentum modes, without imposing momentum-inversion symmetry. The winding number ν_N^{exp} is obtained from the measured pseudospin components and compared with the ideal finite-grid value ν_N on the same APBC momentum grid.

The measured magnetization in Fig. 3(a–d) generally lies below the ideal finite-size result. Averaging $|M_x^{\mathrm{exp}} - M_x^{\mathrm{ideal}}|$ over the 34 parameter points and five runs gives mean absolute deviations of 0.02893 for $N = 16$ and 0.04225 for $N = 32$. The extrema of the fitted derivatives $\partial M_x/\partial\lambda$, where λ denotes the scanned coupling, lie close to those of the ideal finite-size curves. These fit parameters do not establish a change in the thermodynamic-limit transition points. At $\lambda_1 = \lambda_2 = 0$, the measured mean magnetizations are 0.9503 and 0.9354 for $N = 16$ and $N = 32$, respectively, compared with the ideal value of one. Since M_x is obtained by averaging the longitudinal polarization of the momentum modes, imperfect state preparation and population mixing during gate operations can contribute to this reduction. Readout errors also lower the signal for a fully polarized mode: misidentifying $|0\rangle$ as $|1\rangle$ changes its contribution from $+1$ to -1, giving $z_{\mathrm{meas}} = 1 - 2e_0$, where $e_0 = P(1 \mid 0)$.

The measured winding numbers follow the ideal finite-grid values [Fig. 3(e–h)]. At every parameter point and for both system sizes, the majority of the five runs gives the ideal finite-grid value ν_N. The resulting sequence is $0 \to 1$ along the λ_1 scan and $2 \to 0 \to 1 \to 2$ along the λ_2 scan. Individual runs yield 169 of 170 correct results for $N = 16$ and 168 of 170 for $N = 32$, or 337 of 340 (99.1%) in total. The three errors occur in the λ_2 scan at $\lambda_1 = 0.5$: one run at $N = 16$, $\lambda_2 = 0.58$ gives $\nu_N^{\mathrm{exp}} = 0$ instead of $\nu_N = 1$, and two runs at $N = 32$, $\lambda_2 = -1.02$ give $\nu_N^{\mathrm{exp}} = 1$ instead of $\nu_N = 2$.

Magnetization depends on the longitudinal pseudospin components, whereas the winding number depends on phase differences between neighboring pseudospins on the finite momentum grid. For neighboring momenta k_m and k_{m+1}, the phase increment is evaluated as $\Delta_m = \mathrm{Arg}(s_{m+1}s_m^*)$ with $\mathrm{Arg} \in (-\pi, \pi]$. When the corresponding pseudospins are nearly antiparallel, $|\Delta_m|$ approaches π. A small directional error can then cause the phase difference to cross an endpoint of this interval. For example, an angle increasing past $+\pi$ is represented by a value just above $-\pi$: its principal value decreases by 2π, and the winding number in Eq. (7) decreases by one. This discontinuity follows from the principal-value convention, even when the pseudospin directions vary continuously.

In the three erroneous runs, the affected pseudospins have ideal phase differences of 2.9777 rad

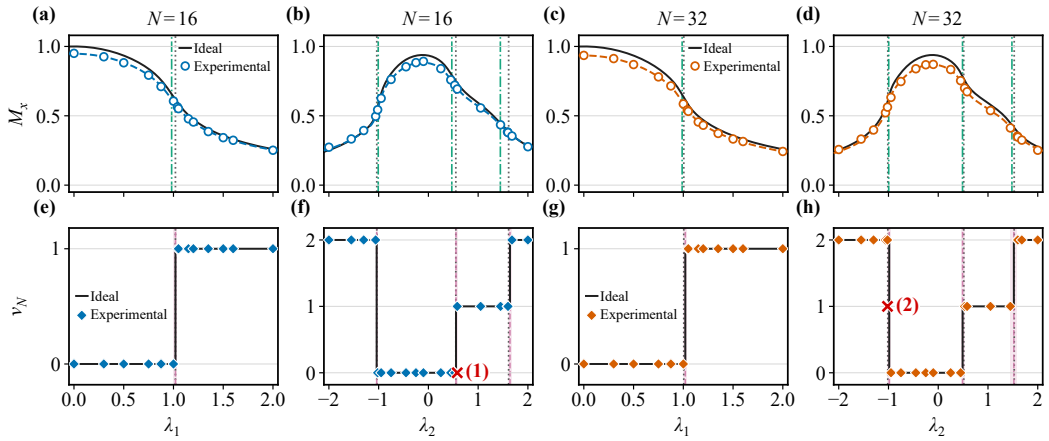


Fig. 3. Transverse magnetization and winding number measured on Tianyan-176. Black solid curves show the ideal finite-size results on the corresponding APBC momentum grids. Panels (a,b,e,f) show $N = 16$, and panels (c,d,g,h) show $N = 32$. The λ_1 scan is taken at $\lambda_2 = 0$, and the λ_2 scan at $\lambda_1 = 0.5$. **(a–d)** Transverse magnetization M_x. Open circles show the mean values over five experimental runs, and dashed curves show the fitted results. Green dash-dotted vertical lines mark the extrema of the fitted derivatives. **(e–h)** Ideal finite-grid winding number ν_N and experimental winding number ν_N^{exp}. Diamonds denote the most frequent value among five runs. Red crosses indicate incorrect values, with the number of occurrences shown in parentheses. Gray dotted vertical lines mark the transitions of the ideal finite-grid winding number ν_N in all panels, and magenta bands indicate the intervals between adjacent sampled points in which the most frequent experimental value changes.

for $N = 16$ and 3.0541 rad for $N = 32$, leaving angular distances of 0.164 and 0.0875 rad to π, respectively. The measured directional errors increase these differences beyond $+\pi$, reducing ν_N^{exp} by one relative to ν_N. All sampled pseudospin magnitudes remain nonzero, excluding an undefined phase at an individual momentum as the origin of these errors. To describe how close neighboring pseudospins are to being antiparallel, we define

$$\phi = \min_m [\pi - |\Delta_m|] = \pi - \max_m |\Delta_m|. \qquad (8)$$

A smaller ϕ therefore requires a smaller change in a neighboring phase difference to cross $+\pi$ or $-\pi$ [Fig. 4(a)]. For nonzero pseudospins with $\phi > 0$, the finite-grid winding number remains unchanged if $\max_m |\delta\Delta_m| < \phi$, provided that the pseudospins remain nonzero. Here $\delta\Delta_m$ is the change in the phase difference between adjacent momenta, evaluated by continuous phase unwrapping before reduction to $(-\pi, \pi]$. This condition excludes crossings of either endpoint and the associated 2π jumps.

Figure 4(c) shows the ideal angular distance ϕ along the λ_1 scan at $\lambda_2 = 0$. It decreases near the finite-grid winding-number transition. Its dependence on system size varies with the coupling [Fig. 4(d)]. At a fixed gapped point away from the transition, ϕ approaches π as the momentum grid is refined. Near the transition, the dependence can be nonmonotonic, as illustrated by the $\lambda_1 = 0.99$ curve. For $\lambda_1 = 0.99$, increasing N moves the finite-grid winding-number transition towards the critical value $\lambda_1 = 1$, closer to the fixed coupling. The two adjacent pseudospins nearest zero momentum initially become more nearly antiparallel, so ϕ decreases. Since the gap at this coupling is nonzero, the pseudospin direction varies continuously with momentum. Once the momentum grid is sufficiently fine, adjacent pseudospin directions become closer and ϕ increases.

To examine winding-number errors under a controlled noise model, we simulate single- and two-qubit depolarizing gate noise along the λ_1 scan at $\lambda_2 = 0$, with infidelities $\varepsilon_1 = 0.017$ and $\varepsilon_2 \approx 6.45\varepsilon_1$, respectively. These rates are used only for this controlled test and are not the calibrated rates used below. Depolarizing noise provides a controlled test with isotropic gate errors and no readout bias, so that the same local rates can be compared across system sizes. For each parameter point, 1,000 simulated data sets are generated with 1,000 shots in each measurement basis. A result is counted as an error if the winding number is undefined or differs from the ideal finite-grid value ν_N. The resulting error fractions estimate P_{err}, with Wilson 95% confidence intervals. The largest observed fractions occur at $\lambda_1 = 1$: 0.3% for $N = 16$ and 9.1% for $N = 32$ [Fig. 4(b)]. Their concentration near the transition coincides with the smaller ϕ in panel (c). This controlled λ_1 scan tests how noise drives neighboring phase differences across $\pm\pi$; it is not intended to reproduce the three errors observed in the hardware data on the λ_2 scan.

At $\lambda_1 = 1$, the finite-grid transition at $\lambda_1 = 1/\cos(\pi/N)$ approaches the sampled point as N increases, reducing ϕ. With the same local gate-noise rates and number of shots, a smaller directional fluctuation can then carry the phase difference past π [Fig. 4(b)]. The increase in the error fraction

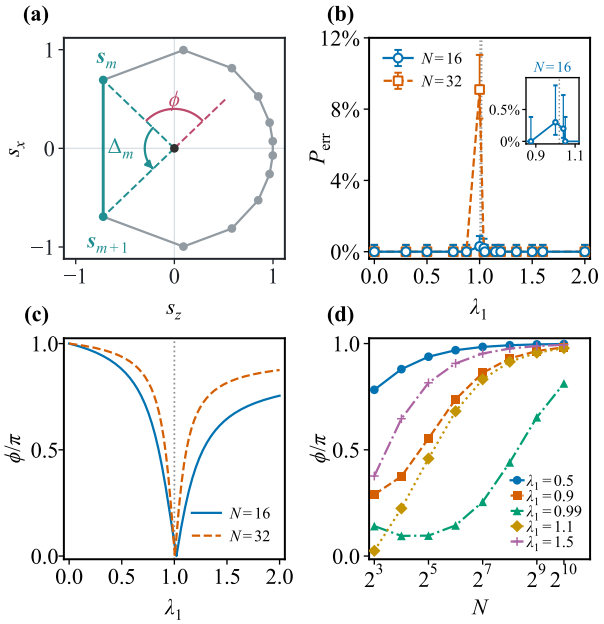


Fig. 4. Angular distance to antiparallel pseudospin directions and winding-number errors along the λ_1 scan at $\lambda_2 = 0$. **(a)** Geometric definition of $\phi = \pi - \max_m |\Delta_m|$, where $\Delta_m = \mathrm{Arg}(s_{m+1} s_m^*)$, for normalized pseudospins in the (s_z, s_x) plane. The highlighted pair has the largest $|\Delta_m|$. **(b)** Winding-number error probability $P_{\rm err}$ for depolarizing gate noise with $\varepsilon_1 = 0.017$ and $\varepsilon_2 \approx 6.45\varepsilon_1$. Each point is obtained from 1,000 independent simulated data sets with 1,000 shots in each measurement basis. Error bars are Wilson 95% confidence intervals. Undefined winding numbers and values different from the ideal ν_N are counted as errors. Circles and solid lines correspond to $N = 16$; squares and dashed lines correspond to $N = 32$. The inset shows the $N = 16$ results near $\lambda_1 = 1$ on an expanded vertical scale. **(c)** Ideal ϕ/π for $N = 16$ and 32. **(d)** Finite-size dependence of ϕ/π at the specified λ_1 values. The dotted vertical line in (c) indicates the thermodynamic-limit transition at $\lambda_1 = 1$, while the dotted lines in (b) indicate the finite-grid transitions at $\lambda_1 = 1/\cos(\pi/N)$.

therefore cannot be attributed solely to noise accumulation with increasing system size.

To separate finite-shot fluctuations from noise-induced changes in the mean pseudospin directions, we vary the gate noise strength and the number of shots S in each measurement basis. We compare $\lambda_2 = 0.58$ and 0.62 at $N = 16$, $\lambda_1 = 0.5$, both with ideal $\nu_N = 1$. A winding-number error was observed experimentally at the first point. The second point has a larger ϕ. Both use the same physical qubits and noise parameters.

For this comparison, effective amplitude damping supplies a simple nonunital channel that can systematically change the mean pseudospin directions. Its strengths are matched to the calibrated gate infidelities within the assumed channel model; these infidelities do not uniquely identify the physical noise channels. Asymmetric readout errors remain fixed at the reference calibration values throughout the scan, including at zero scaled gate infidelity. Scaling all gate infidelities by a common factor preserves the relative rates among qubits and couplers. We parameterize the noise strength by the median single-qubit gate infidelity ε_1, with the calibrated value $\varepsilon_1^{(0)} = 0.00115$. The noisy outcome probabilities, including readout errors, give the mean measured pseudospin components. These are the values approached as the number of shots increases, and their directions determine the limiting winding number. Multinomial sampling of the outcome probabilities yields the winding-number distribution at finite shot number S. The transition thresholds below are predictions of this effective model.

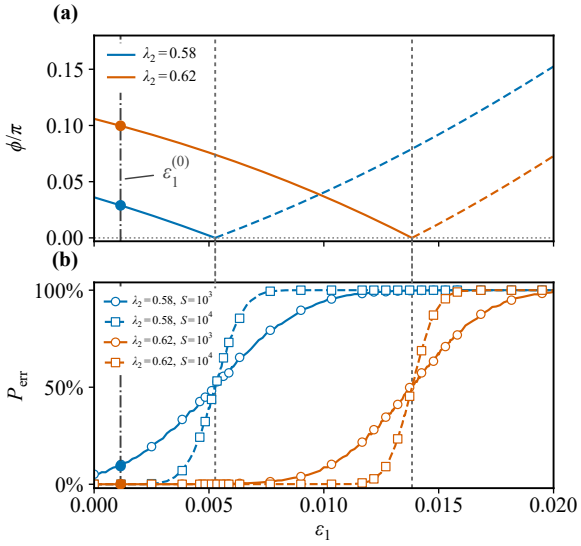


Fig. 5. Effective-model predictions for winding-number errors under amplitude damping and fixed readout errors for $N = 16$ and $\lambda_1 = 0.5$. Blue and orange correspond to $\lambda_2 = 0.58$ and 0.62, respectively. Gate infidelities are scaled proportionally, with ε_1 the median single-qubit gate infidelity. **(a)** Minimum angular distance ϕ/π to antiparallel directions from the mean pseudospins of the noise model. Solid and dashed segments correspond to winding numbers 1 and 0, respectively. Gray vertical dashed lines mark the noise strengths at which the model predicts a change in the winding number. **(b)** Error fraction relative to the ideal finite-grid value $\nu_N = 1$, including undefined results. Each point uses 10,000 independent samples, with S shots in each measurement basis. Dash-dotted vertical lines and filled circles mark the calibrated reference $\varepsilon_1^{(0)} = 0.00115$, with $S = 1000$ in (b). Readout errors remain present at $\varepsilon_1 = 0$.

In the effective model of Fig. 5(a), the winding number calculated from the mean measured pseudospins remains 1 until the directions at two neighboring sampled momenta become antiparallel. Their phase difference then passes through π, and the winding number changes to 0. All sampled pseudospin magnitudes remain nonzero. As the noise strength increases further, the directions move away from antiparallel and ϕ increases again, while the winding number remains 0 over the displayed range. Thus $\phi > 0$ does not by itself establish agreement with the ideal finite-grid winding number. For $\lambda_2 = 0.58$ and 0.62, the model

predicts the first winding changes at $\varepsilon_1 \simeq 0.005271$ and 0.013838, respectively.

Finite-shot errors remain possible while the mean pseudospins have the ideal winding number. At the calibrated reference, the winding number is 1 at both points, with $\phi/\pi = 0.02895$ and 0.09971 for $\lambda_2 = 0.58$ and 0.62, respectively. For $S = 10^3$, the error fraction is 9.39% at the smaller-ϕ point, whereas no errors are found in 10,000 reconstructions at the larger-ϕ point [Fig. 5(b)]. For $S = 10^4$, no errors are found at either point.

First-order propagation of uncertainty, including correlations between estimates obtained from the same counts, gives similar phase uncertainties at the two points. For comparable phase fluctuations, the probability of crossing π is therefore higher at the point with smaller ϕ. At fixed noise parameters, the covariance of the component estimates scales as S^{-1}, giving phase standard deviations proportional to $S^{-1/2}$ within this approximation. The plotted error fractions are obtained by sampling the full joint outcome probabilities.

At fixed noise strength, finite-shot fluctuations decrease as S increases. If the mean pseudospins have the ideal winding number, the error fraction decreases with increasing S. If noise changes their winding number from 1 to 0, the reconstructed winding approaches 0 as S increases, and the error fraction relative to the ideal $\nu_N = 1$ approaches unity. The sharper $S = 10^4$ curves in Fig. 5(b) follow from this behavior. Increasing S reduces statistical fluctuations, but does not remove the noise-induced change in the mean winding number.

4. Conclusion

We measured the transverse magnetization and winding number of an extended TFIC with three-spin interactions using shallow momentum-pair circuits. Each $(k, -k)$ pair is prepared with one single-qubit rotation and one entangling gate, and measurements in the Z and X bases provide the longitudinal components and XX correlations. Experiments on Tianyan-176 with $N = 16$ and $N = 32$ give winding numbers 0, 1, and 2 on the finite momentum grids. Although the measured magnetization deviates from the ideal values, 337 of 340 individual runs give the ideal finite-grid winding number. The three incorrect values occur when neighboring pseudospins are nearly antiparallel. Small directional errors can then drive the principal phase difference across $\pm\pi$, changing the finite-grid winding number by one while the pseudospin magnitudes remain nonzero. The angular margin ϕ quantifies this sensitivity: a smaller ϕ requires a smaller phase fluctuation to change the winding number. Noise simulations further separate finite-shot fluctuations from systematic changes of the mean pseudospins. Finite-shot errors may occur even when the mean pseudospins have the ideal winding number and decrease as the number of shots is increased. Once noise changes the winding number of the mean pseudospins, however, increasing the number of shots does not recover the ideal value.

The present momentum-pair circuits rely on translational invariance. Weak impurities break this symmetry and couple different momenta, so the momentum pairs can no longer be treated independently. Extending the method would require a more general state-preparation circuit, while the winding number could be calculated in real space [32].

Supplementary material

See the supplementary material for the model mapping and measurement estimators (Sec. S1), details of the noise simulations and statistical analysis (Sec. S2), and the magnetization fits (Sec. S3).

Data availability statement

The data that support the findings of this article are available from the corresponding author upon reasonable request.

Acknowledgment

K. Liu acknowledges support from the Postgraduate Research & Practice Innovation Program of Nanjing University of Aeronautics and Astronautics (NUAA) under Grant No. xcxjh20252119. W.-L. You acknowledges support from the National Natural Science Foundation of China under Grant No. 12674184 and from NUAA under Grant No. 1018-ILF26028. This work was also supported in part by the Tianyan Quantum Computing Cloud Platform developed by China Telecom Quantum Information Technology Group Co., Ltd.

References

[1] Pfeuty P 1970 *Ann. Phys.* **57** 79–90

[2] Su Z, Jiang Y, Hu G, Su Y H, Li L, You W L, Liu M and Chen X 2025 *Chin. Phys. B* **34** 086401

[3] Verstraete F, Cirac J I and Latorre J I 2009 *Phys. Rev. A* **79** 032316

[4] Cervera-Lierta A 2018 *Quantum* **2** 114

[5] Preskill J 2018 *Quantum* **2** 79

[6] Xu K and Fan H 2022 *Chin. Phys. B* **31** 100304

[7] Farreras M and Cervera-Lierta A 2025 *SciPost Phys. Lect. Notes* **95**

[8] Boyajian W L, Murg V and Kraus B 2013 *Phys. Rev. A* **88** 052329

[9] Hebenstreit M, Alsina D, Latorre J I and Kraus B 2017 *Phys. Rev. A* **95** 052339

[10] Kökcü E, Camps D, Oftelie L B, Freericks J K, de Jong W A, Beeumen R V and Kemper A F 2022 *Phys. Rev. A* **105** 032420

[11] Guo X Y, Yang C, Zeng Y, Peng Y, Li H K, Deng H, Jin Y R, Chen S, Zheng D and Fan H 2019 *Phys. Rev. Applied* **11** 044080

[12] Hang Y, Di Felice R, Nakano A and Haas S 2026 *Phys. Rev. B* **113** 235145

[13] Xiao T, Xie D, Dong Z, Chen T, Yi W and Yan B 2021 *Sci. Bull.* **66** 2175–2180

[14] Wang Y, Zhang J H, Li Y, Wu J, Liu W, Mei F, Hu Y, Xiao L, Ma J, Chin C and Jia S 2022 *Phys. Rev. Lett.* **129** 103401

[15] Liang Q, Dong Z, Pan J S, Wang H, Li H, Yang Z, Yi W and Yan B 2024 *Nat. Phys.* **20** 1738–1743

[16] Niu Y, Chung S B, Hsu C H, Mandal I, Raghu S and Chakravarty S 2012 *Phys. Rev. B* **85** 035110

[17] Zhang G and Song Z 2015 *Phys. Rev. Lett.* **115** 177204

[18] Zhang G, Li C and Song Z 2017 *Sci. Rep.* **7** 8176

[19] Nie W, Mei F, Amico L and Kwek L C 2017 *Phys. Rev. E* **96** 020106(R)

[20] Ding C 2019 *Phys. Rev. E* **100** 042131

[21] Surace J and Tagliacozzo L 2022 *SciPost Phys. Lect. Notes* **54**

[22] Tan Z, Wang K, Yang S *et al.* 2026 *Commun. Phys.* **9** 136

[23] Zheng W, Xu J, Ma Z, Li Y, Dong Y, Zhang Y, Wang X, Sun G, Wu P, Zhao J, Li S, Lan D, Tan X and Yu Y 2022 *Chin. Phys. Lett.* **39** 100202

[24] Zhou K, Xu J W, Su Q P, Zhang Y, Yu X M, Ma Z, Zhang H Y, Shi H Y, Zheng W, Pan S, Kang Y, Huang Z, Yang C P, Li S X and Yu Y 2025 *Phys. Rev. Lett.* **135** 250601

[25] Huai S, Lin L, Bu K, Cai T, Zong Z, Yang X, Li Y, Ye Y, Zhang Z, Zhang S and Lee C 2026 arXiv:2610.09673 [quant-ph]

[26] Xiao X, Freericks J K and Kemper A F 2021 *Quantum* **5** 553

[27] Xiao X, Freericks J K and Kemper A F 2023 *Quantum* **7** 987

[28] Tianyan Quantum Group 2025 arXiv:2512.10504 [quant-ph]

[29] Tu Z, Xu J, Zhou X, Zhu Y, Liu Y, Du Q, Lian H and Zhou B 2025 *Mach. Learn.: Sci. Technol.* **6** 045033

[30] Lieb E, Schultz T and Mattis D 1961 *Ann. Phys.* **16** 407–466

[31] Nielsen M A and Chuang I L 2010 *Quantum Computation and Quantum Information: 10th Anniversary Edition* (Cambridge: Cambridge University Press)

[32] Lin L, Ke Y and Lee C 2021 *Phys. Rev. B* **103** 224208